Electron Microscopic Study of the Influence of Annealing on Ge–Sb–Te Thin Films Obtained by Vacuum Thermal Evaporation

Yu. S. Sybina[a, *], **N. I. Borgardt**[a], **P. I. Lazarenko**[a], **V. S. Parsegova**[a],
A. S. Prikhodko[a], **and A. A. Sherchenkov**[a]

[a]*National Research University of Electronic Technology (MIET), Moscow, 124498 Russia*
*e-mail: julia3ybina@gmail.com
Received November 29, 2018; revised January 16, 2019; accepted February 11, 2019

Abstract—Using transmission electron microscopy it is demonstrated that the annealing of amorphous $Ge_2Sb_2Te_5$ films deposited by vacuum thermal evaporation at 250°C leads to the formation of a hexagonal phase with a peculiar block structure. Herewith, island defects are formed on their surface representing the cubic modification of Sb_2O_3. The sizes of these defects and portion of the surface area occupied by them are estimated using images of scanning electron microscopy. The formation of antimony-oxide crystallites can be attributed to enrichment of the surface area of the initial film with antimony which is oxidized during annealing. Due to the formation of defects, the film composition in adjacent local areas varies and becomes close to the stoichiometric values for $Ge_3Sb_2Te_6$.

Keywords: phase change memory, thin films, Ge–Sb–Te, surface defects, scanning electron microscopy (SEM), transmission electron microscopy (TEM), energy dispersive X-ray spectroscopy (EDS)

DOI: 10.1134/S1027451019050380

INTRODUCTION

Phase change memory (PCM) based on Ge–Sb–Te (GST) chalcogenide semiconductors is a promising type of data storage [1]. The principle of Boolean logic is implemented on the basis of various material phase states (amorphous and crystalline), the transition between which is performed under the impact of an optical or electric pulse. Among the numerous GST compounds $Ge_2Sb_2Te_5$ (GST225) material attracts the greatest attention due to a combination of functionally significant properties: time of phase transition, number of rewriting cycles, melting point determining the power consumption [2].

The most popular production methods of GST films are magnetron sputtering [3], vacuum thermal evaporation (VTE) [4], gas-phase deposition [5], as well as molecular-beam epitaxy [6]. The epitaxial production methods of GST layers with a perfect crystalline lattice are highly promising for studying fundamental processes which occur upon phase transitions in PCM materials. The advantages of vacuum thermal evaporation are the relatively simple technology and cost efficiency as well as the possibility of varying the chemical composition of the sputtered film, which interest in using this method to produce GST films, especially at the stage of technology adjustment.

Among the numerous methods of studying GST thin films, transmission electron microscopy (TEM) [7, 8] and energy-dispersive X-ray spectroscopy (EDS) [9] which allow the investigation of local variations in the structure and composition occurring upon solidification including the formation of various phases [9–11], play a special role. With their help, it was revealed that the described phase separation can be attributed to an increase in the density of GST material by 7–9% upon solidification and, respectively, a decrease in the cell volume [12]. The relaxation of stresses that arise leads to segregation [9].

Using SEM and TEM as well as atomic-force microscopy surface formations (defects) have been detected in chalcogenide systems [5, 6, 13]; the causes of their formation have been barely studied. Such defects in the form of truncated tetrahedrons with the sizes reaching several hundreds of nanometers can lead to the degradation of PCM devices. It should be mentioned that the thin films studied in [5, 6, 13] were grown by epitaxial methods, whereas for films produced by VTE such defects have not been studied yet.

This work is devoted to structural and analytical studies of the influence of annealing at 250°C on GST225 thin films produced by VTE; heat treatment of these films results in their phase transition from the amorphous to crystalline state. The structure and chemical composition of GST films as well as surface defects formed after annealing are studied by TEM and EDS. The average sizes of these defects and portion of the surface area occupied by them are determined by the digital processing of SEM images.

THIN-FILM FORMATION AND EXPERIMENTAL FACILITIES

GST225 Thin-Film Formation

Initial polycrystalline $Ge_2Sb_2Te_5$ powder was synthesized by fusing materials of the corresponding elements in vacuum quartz ampoules [11]. Thin films were formed on thermally oxidized silicon substrates by vacuum thermal evaporation of the synthesized powder under a residual pressure of less than 4×10^{-5} mm Hg. A quartz crucible with a narrow neck was used as an evaporator with a heating coil around its periphery. Two stage heating was applied for evaporation. During the first stage aimed at degassing the evaporated powder, it was heated from ambient temperature to 300°C at an average rate of 25 K/min with subsequent holding for 10 min. During the second stage, the electric current passing across the heater sharply increased and the temperature in the quartz ampoules exceeded 750°C. The synthesized powder was evaporated in the so called "explosive" mode. The substrate temperature during deposition did not exceed 50°C which facilitated the production of thin films in the amorphous state. The film thickness was monitored by reference samples using an Alpha-Step D-120 stylus profiler and approximately equaled 150 nm. The amorphous films were annealed in a PL-20 convection furnace at 250°C for 15 min, homogeneous heating to this temperature at a rate of 15 K/min was supported by a proportional−integral−derivative (PID) controller. The substrates were cooled naturally in the convection furnace after it was switched off.

Experimental Facilities

The structure and composition of the GST thin films were analyzed at an accelerating voltage of 200 kV in a Titan Themis 200 transmission electron microscope equipped with a Super-X energy-dispersive spectrometer. Thin foils for TEM were prepared by means of focused ion beam according to the standard procedure In-Situ Lift-Out [14, 15] in a Helios NanoLab 650 electron ion microscope equipped with an injector of $C_9H_{10}Pt$ organometallic compound for the local deposition of platinum and a Kleindiek MM3A-EM micromanipulator [16]. The surface morphology of the GST films was studied using the microscope's electron column at an accelerating voltage of 1 kV and a beam current of 100 pA. The best resolution of secondary-emission images was obtained by the immersion mode of an objective lens. The digital processing of experimental microimages was performed using Matlab software.

RESULTS AND DISCUSSION

Initial GST film

TEM analysis of the transverse cross section of the grown film demonstrated that its structure is homogeneous both on the direction of growth along the z axis
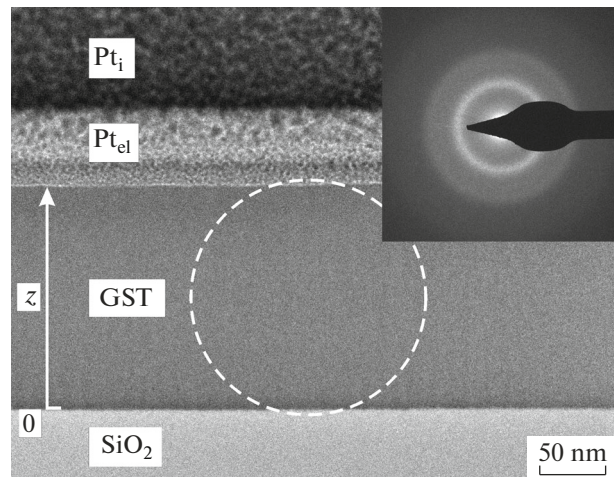

Fig. 1. TEM image of the initial GST film and diffraction pattern (insertion) of the area highlighted by a dashed line evidencing its amorphous structure. Protective layers deposited upon the production of the thin foil by electron and ion beams are denoted as Pt_{el} and Pt_i. The z axis shows the direction of film growth.

and in the lateral direction (Fig. 1). The amorphous state of the film was evidenced by a diffraction pattern formed using a selector aperture in order to obtain structural data only for the GST area highlighted by the dashed circle in the TEM image (Fig. 1).

The concentrations of germanium, antimony, and tellurium obtained by EDS and averaged across the entire thickness of the GST film deviated by no more than 2 at % from the stoichiometric values for the GST225 compound. In addition, the concentration profiles along the growth direction determined by averaging their 2D distributions evidenced the significant gradient of Sb and Te concentrations in GST. As seen in Fig. 2a, during layer growth the antimony content increased from about 6 to 60 at %, and the tellurium content decreased from 75 to 30 at %; herewith, the Ge content varied to a lesser degree and was in the range of 12−26 at %.

The film-surface morphology analyzed by SEM prior to preparation of the transverse cross section for TEM demonstrates that the film surface was rather smooth (without any visible defects).

The detected heterogeneity of the chemical composition of the GST film could be attributed to a significant difference in the pressures of vaporized Sb [17], Te [18], and GeTe [19] and Sb_2Te_3 [20], which could be formed at the evaporation point as a consequence of GST225 decomposition. Hence, upon evaporation of the synthesized powder the compositions of the vapor phase and, respectively, growing film varied over time. At first the fraction enriched with Te was predominantly deposited characterized by higher pressure of vapors. The fraction enriched with Sb and characterized by the lowest vapor pressure was deposited in the final stage of film growth.
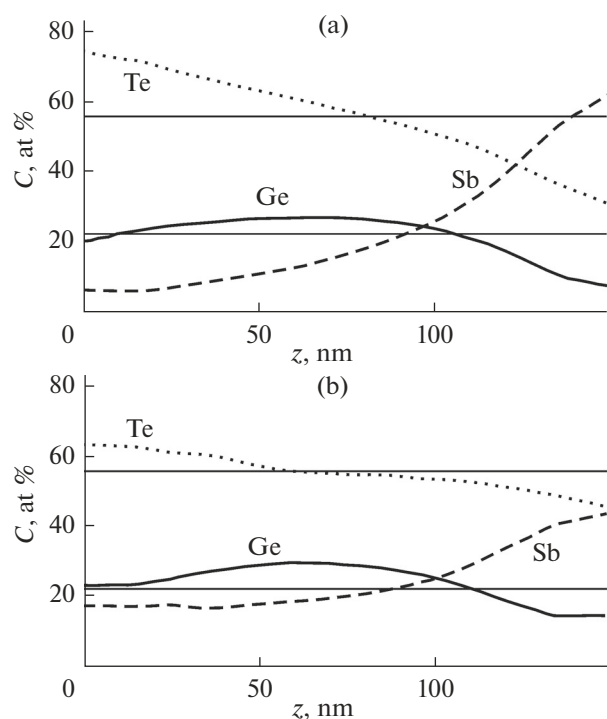
Fig. 2. Concentration profiles for Ge (solid line), Sb (dashed line), Te (dotted line) for the initial (a) and annealed (b) films along the growth direction. Horizontal lines correspond to stoichiometric concentrations of Ge and Sb (22.2 at %) as well as Te (55.6 at %) for GST225 compound.

Fig. 3. HREM image of the GST film after annealing with a peculiar crystalline block structure. One block is highlighted by white rectangle.

GST Film Structure and Composition after Annealing

The electron microscopic study of a heat-treated GST225 film demonstrated that annealing at 250°C leads to a phase transition from the amorphous to crystalline state as illustrated in Fig. 3 showing a high-resolution electron microscopic image (HREM). According to [7, 8, 21] the visualized block structure is peculiar for the GST hexagonal phase; herewith, the blocks are separated by so called van der Waals gaps which are formed in the (0001) planes. The distance between two adjacent gaps determines the lattice constant c of the real GST compound. The maximum size of the blocks reaches 3 nm; herewith, 17 atomic planes are positioned between two adjacent gaps [21]. The GST composition in the block is described by the general formula $Ge_xSb_2Te_{3+x}$, whereas in the [0001] direction the tellurium atomic planes alternate with planes filled with atoms of germanium and antimony in various ratios [8].

In the HREM image of the annealed GST film (Fig. 3) the van der Waals gaps indicated by arrows have dark contrast. The sizes of the GST blocks determined upon image analysis and equaling the lattice constant c for most blocks equaled 2 nm, which corresponds to $Ge_3Sb_2Te_6$ (GST326) (blocks marked by *2* in Fig. 3). In addition compounds with lattice constants of 1.7 and 2.4 nm were detected (*1* and *3* in Fig. 3),
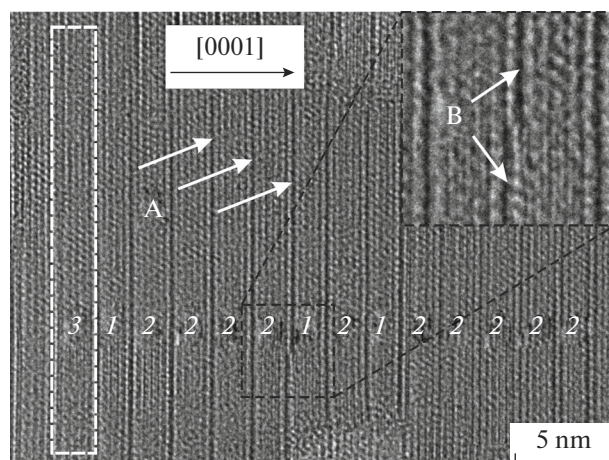
which can correspond to GST225 and $Ge_4Sb_2Te_7$. A peculiar feature is comprised of variations in the block size in the (0001) plane leading to local displacement of the van der Waals gap as illustrated in the insert (Fig. 3).

The chemical composition in the film local area is determined by the combination of constituent GST blocks which made it possible to estimate the variations that occurred upon film annealing. The formation of numerous GST326 blocks in the film with stoichiometry in the initial amorphous phase close to GST225 evidences a trend toward a decrease in the antimony content in the film upon annealing.

The HREM results correlate with the EDS data according to which, in local areas of the film located near surface defects (see below), the following concentrations were obtained: 28.9 for Ge, 17.6 for Sb, and 53.5 at % for Te, which is close to the theoretical values for GST326. In other areas annealing did not lead to variations in the average chemical composition of the film, the concentrations of elements corresponded to stoichiometry of the GST225 compound.

The gradient in the average distributions of Sb and Te along the growth direction revealed in the initial amorphous film remained after annealing, though the differences in the concentrations of antimony and tellurium in the top and bottom areas of the GST layer decreased (Fig. 2b).

Surface Defects

Annealing of the GST film also resulted in significant variations in the surface morphology revealed by SEM (Fig. 4). Defects were formed on it as arbitrarily located island formations of complex shape, quite often close to truncated tetrahedrons and octahedrons. Their lateral sizes varied in the range of 0.3–1.4 μm; some defects are indicated by arrows in Fig. 4.
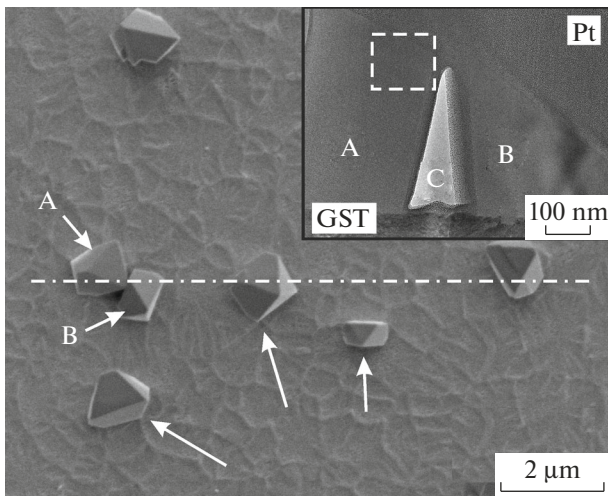
Fig. 4. SEM image of the GST film after annealing with surface defects indicated by arrows. The insert illustrates a TEM image of the transverse cross section of the film taken along the dashed line with defects A and B. Letter C denotes a cavity between the defects.
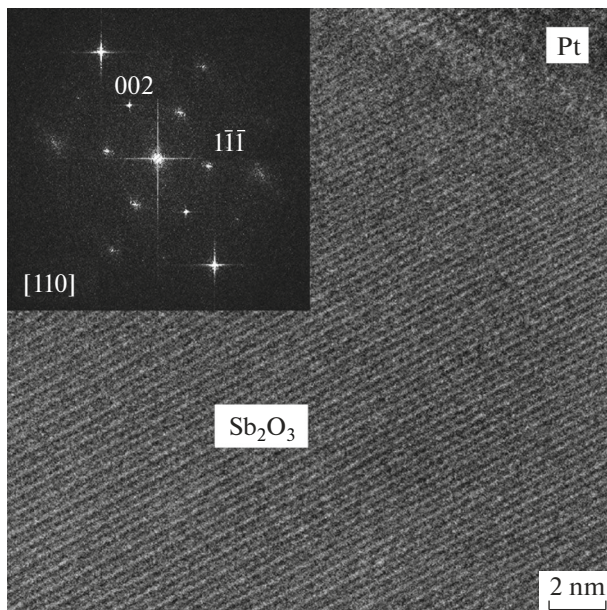

Fig. 5. HREM image of the area of defect A in the orientation (110) highlighted by a dashed line in Fig. 4 and its Fourier transform (insertion).

In order to estimate the average area of surface defects of the GST film, SEM images were digitally processed using Matlab software. During the first stage experimental microimages were binarized using a histogram of the intensity distribution. Its analysis made it possible to detect the range of intensity corresponding to surface defects. In the next stage the obtained binary image was used to highlight the contours of certain defects using the method of coupled compo-

nents with a connectivity criterion based on eight neighbors [22], then their areas were calculated. In the last stage using a selection of about 650 defects it was established that their average area was about 0.1 μm^2 and the part of surface area occupied by them was about 1%.

Analysis of the structure and chemical composition of surface defects using the procedure of In-Situ Lift-Out was performed with an electron microscopic sample which contained one thin foil transverse cross section along the direction shown in Fig. 4 by the dash and dot line. Due to such an approach it was possible to compare the SEM and TEM images of some defects (indicated by A and B in Fig. 4) and to establish that the height of surface formations which could reach several hundreds of nanometers is comparable with their lateral sizes and significantly exceeds the thickness of the GST film.

In order to reveal the structure of defects, HREM images were acquired and their Fourier analysis was performed. Such an image for a defect in the orientation (110) is exemplified in Fig. 5 with the respective Fourier transform in the insert. It follows that the defect is characterized by a cubic lattice with the constant $a = 1.11$ nm. Chemical analysis in the region illustrated in the insert (Fig. 4), revealed that the defects contain about 41 at % antimony and 59 at % oxygen; their ratio corresponds to the stoichiometry of antimony oxide Sb_2O_3. The absence of germanium and tellurium in the defects evidences that they are not the GST material.

The results of the analysis of HREM images and EDS data make it possible to conclude that the surface formations which resulted from annealing are crystallites of senarmontite Sb_2O_3 with a cubic lattice [23, 24]. They are similar to Sb_2O_3 crystals of cubic modification described in [23, 25] occurring on the surface of antimony oxide after heat treatment and having a shape close to a tetrahedron or octahedron.

The formation of the revealed Sb_2O_3 crystallites could be attributed to the heterogeneous distribution of chemical elements in the GST film, the top part of which is enriched with antimony. As a consequence of oxidation during annealing defects containing Sb are formed on its surface [26]. Herewith, the antimony concentration in the bulk of the GST layer decreases which agrees with the TEM and EDS data, according to which its average composition in local areas in the vicinity of surface defects becomes close to the stoichiometry of GST326 with a lower antimony concentration in comparison with the initial amorphous film corresponding on average to the GST225 compound.

CONCLUSIONS

The structure and composition of both initial Ge–Sb–Te thin films and those annealed at 250°C were studied using SEM and TEM as well as X-ray spectral microanalysis. It has been revealed that the initial GST film was in the amorphous state, its average com-

position was the same as that of GST225, however, in the growth direction it is characterized by a significant increase in the Sb content and a decrease in the Te content which could be attributed to the peculiarities of film formation by vacuum thermal evaporation. During annealing the film material was solidified with the formation of a block structure peculiar for the GST hexagonal phase, defects were formed on its surface with a shape close to a truncated tetrahedron or octahedron and the average chemical composition in local areas adjacent to defects varied and corresponded to GST326.

Using the digital processing of SEM images it has been determined that the sizes of surface defects varied in the range of $0.3-1.4$ μm, its average surface area was about 0.1 μm^2, and the portion of surface occupied by them equaled 1%. Using high-resolution electron microscopic images and X-ray microanalysis it was demonstrated for the first time that such defects are crystallites of senarmontite: a cubic modification of antimony oxide Sb_2O_3 with the lattice constant $a = 1.11$ nm. Their occurrence can be attributed to enrichment of the surface layer of the initial amorphous film with antimony, the oxidation of which under the action of annealing leads to the occurrence of Sb containing island formations and modification of the average chemical composition of the film.

REFERENCES

1. *Phase Change Memory,* Ed. by A. Redaelli (Springer International, Cham, 2018).
https://doi.org/10.1007/978-3-319-69053-7

2. S. A. Kozyukhin, A. A. Sherchenkov, V. M. Novotortsev, and S. P. Timoshenkov, Nanotechnol. Russia **6**, 227 (2011).

3. T. H. Jeong, M. R. Kim, H. Seo, et al., J. Appl. Phys. **86** (2), 774 (1999).
https://doi.org/10.1063/1.370803

4. P. Kumar, S. K. Tripathi, and I. Sharma, J. Alloys Compd. **755**, 108 (2015).
https://doi.org/10.1016/j.jallcom.2018.04.316

5. M. Schuck, S. Ries, M. Schreiber, et al., J. Cryst. Growth **420**, 37 (2015). .
https://doi.org/10.1016./j.jcrysgro.2015.03.034

6. J. E. Boschker and R. Calarco, Adv. Phys. X **2** (3), 675 (2017).
https://doi.org/10.1080/23746149.2017.1346483

7. Y. J. Park, J. Y. Lee, and Y. T. Kim, Appl. Surf. Sci. **253** (2), 714 (2006).
https://doi.org/10.1016/j.apsusc.2005.12.158

8. B. J. Kooi and J. T. M. De Hosson, J. Appl. Phys. **92** (7), 3584 (2002).
https://doi.org/10.1063/1.1502915

9. L. Krusin-Elbaum, C. J. Cabral, K. N. Chen, et al., Appl. Phys. Lett. **90** (14), 141902 (2007).
https://doi.org/10.1063/1.2719148

10. S. Privitera and E. Rimini, J. Appl. Phys. **94** (7), 4409 (2003).
https://doi.org/10.1063/1.1604458

11. A. Sherchenkov, S. Kozyukhin, N. Borgardt, et al., J. Non-Cryst. Solids **501,** 101 (2017). .
https://doi.org/10.1016/j.jnoncrysol.2017.12.023

12. W. K. Njoroge, H. W. Wöltgens, and M. Wuttig, J. Vac. Sci. Technol., A **20** (1), 230 (2002).
https://doi.org/10.1116/1.1430249

13. I. Hilmi, E. Thelander, P. Schumacher, et al., Thin Solid Films **619,** 81 (2016).
https://doi.org/10.1016/j.tsf.2016.10.028

14. R. L. Volkov, N. I. Borgardt, V. N. Kukin, et al. J. Surf. Invest.: X-Ray Synchrotron Neutron Tech. **5** (5), 900 (2011).

15. Ya. S. Grishina, N. I. Borgardt, R. L. Volkov, et al., J. Surf. Invest.: X-Ray Synchrotron Neutron Tech. **11** (1), 226 (2017).
https://doi.org/10.1134/S102745101701027X

16. T. A. Alekhova, V. Ya. Shklover, N. A. Zagustina, et al., J. Surf. Invest.: X-Ray Synchrotron Neutron Tech. **4** (5), 747 (2010).

17. G. M. Rossenblatt and C. E. Birchenall, J. Chem. Phys. **35** (3), 788 (1961).
https://doi.org/10.1063/1.1701217

18. A. P. Ubelis, J. Eng. Phys. **42** (3), 309 (1982).

19. C. Hirayama, J. Phys. Chem. **66** (8), 1563 (1962).
https://doi.org/10.1021/j100814a519

20. V. Piacente, P. Scardala, and D. Ferro, J. Alloys Compd. **178** (1−2), 101.
https://doi.org/10.1016/0925-8388(92)90251-4

21. A. M. Mio, S. M. S. Privitera, V. Bragaglia, et al., Nanotechnology **28**, 065706 (2017).
https://doi.org/10.1088/1361-6528/28/6/065706

22. R. Gonzalez and R. Woods, *Digital Image Processing* (Prentice Hall, Upper Saddle River, NJ, 1992; Tekhnosfera, Moscow, 2005).

23. R. L. Zhang and S. Z. Tang, Ultrason. Sonochem **22**, 155 (2015).
https://doi.org/10.1016/j.ultsonch.2014.06.021

24. N. Tigau, V. Ciupina, G. Prodan, et al., J. Cryst. Growth **269,** 392 (2004).
https://doi.org/10.1016/j.jcrysgro.2004.05.052

25. T. Cebriano, B. Mendez, and J. Piqueras, CrystEngComm. **18** (14), 2541 (2016).
https://doi.org/10.1039/C6CE00287K

26. X. Wang, M. He, J. Xi, and X. Lu, Microchem. J. **97**, 4 (2011).
https://doi.org/10.1016/j.microc.2010.05.011

Translated by I. Moshkin